



UNIVERSITY OF LEEDS

This is a repository copy of *Characterisation of multiple hindered settling regimes in aggregated mineral suspensions*.

White Rose Research Online URL for this paper:

<https://eprints.whiterose.ac.uk/104615/>

Version: Accepted Version

---

**Article:**

Johnson, M, Peakall, J, Fairweather, M et al. (3 more authors) (2016) Characterisation of multiple hindered settling regimes in aggregated mineral suspensions. *Industrial and Engineering Chemistry Research*, 55 (37). pp. 9983-9993. ISSN 0888-5885

<https://doi.org/10.1021/acs.iecr.6b02383>

---

© 2016 American Chemical Society. This document is the Accepted Manuscript version of a Published Work that appeared in final form in *Industrial and Engineering Chemistry Research*, copyright © American Chemical Society after peer review and technical editing by the publisher. To access the final edited and published work see <http://dx.doi.org/10.1021/acs.iecr.6b02383>. Uploaded in accordance with the publisher's self-archiving policy.

**Reuse**

Items deposited in White Rose Research Online are protected by copyright, with all rights reserved unless indicated otherwise. They may be downloaded and/or printed for private study, or other acts as permitted by national copyright laws. The publisher or other rights holders may allow further reproduction and re-use of the full text version. This is indicated by the licence information on the White Rose Research Online record for the item.

**Takedown**

If you consider content in White Rose Research Online to be in breach of UK law, please notify us by emailing [eprints@whiterose.ac.uk](mailto:eprints@whiterose.ac.uk) including the URL of the record and the reason for the withdrawal request.



[eprints@whiterose.ac.uk](mailto:eprints@whiterose.ac.uk)  
<https://eprints.whiterose.ac.uk/>

# Characterisation of multiple hindered settling regimes in aggregated mineral suspensions

Michael Johnson,<sup>\*,†</sup> Jeffrey Peakall,<sup>‡</sup> Michael Fairweather,<sup>†</sup> Simon Biggs,<sup>¶</sup> David Harbottle,<sup>†</sup> and Timothy N. Hunter<sup>†</sup>

*School of Chemical and Process Engineering, University of Leeds, Leeds, UK, LS2 9JT, School of Earth and Environment, University of Leeds, Leeds, UK, LS2 9JT, and School of Chemical Engineering, University of Queensland, Brisbane, Qld 4072, Australia*

E-mail: [pm12mcj@leeds.ac.uk](mailto:pm12mcj@leeds.ac.uk)

---

\*To whom correspondence should be addressed

<sup>†</sup>University of Leeds

<sup>‡</sup>University of Leeds

<sup>¶</sup>University of Queensland

## Abstract

Aqueous suspensions of magnesium hydroxide are shown to exhibit low zeta potential behaviour and highly complex settling dynamics. Two distinct regimes of hindered settling behaviour are observed either side of a threshold concentration,  $\phi^*$ , of 2.38 % v/v, which is considerably below the gel point,  $\phi_g$ , observed at  $5.4 \pm 1.6$  % v/v. The low concentration regime was characterised by a very large Richardson and Zaki exponent of 146, a factor of 10 larger than that of the high concentration regime. Michaels and Bolger analysis of the low concentration regime implies settling governed by large, low density macro-aggregates of 138-147  $\mu\text{m}$  diameter and low intra-aggregate packing fractions in the order of 0.05, which is in good agreement with *in-situ* particle characterisation undertaken using Particle Vision and Measurement (PVM) and Focused Beam Reflectance Measurements (FBRM). The large macro-aggregates must undergo some shear densification within the higher concentration hindered settling regime in order for the suspension to gel at a concentration of 5.4 % v/v. Consequently, fluid flow past small, shear resistant primary agglomerates, observed within the aggregates using Scanning Electron Microscopy (SEM) and flow particle image analysis (FPIA), during aggregate densification may represent the limiting step for dewatering within the high concentration regime.

## Keywords

hindered settling, aggregation, magnesium hydroxide, Turbiscan, PVM, FBRM

# Introduction

The dynamics of settling suspensions has attracted decades of research due to its significance to mineral processing, water and waste-water treatment industries as well as to natural geophysical processes<sup>1-3</sup>. For fine, cohesive mineral systems often encountered in industrial thickening<sup>4</sup>, van der Waals forces exceed the particle weight by orders of magnitude<sup>5,6</sup> and hence particles of low surface potential exist as aggregates in suspension<sup>7,8</sup>. Polydisperse, fractal aggregates have exhibited highly complex settling behaviour in various mineral suspensions, including aqueous suspensions of calcium carbonate<sup>9</sup>, magnesium hydroxide<sup>10</sup>, titanium dioxide<sup>11</sup> and kaolinite<sup>12</sup>. The observed increase in drag on the settling phase with increased concentration, or hindering effects, can be orders of magnitude greater than observed in suspensions of uniform hard spheres<sup>9</sup>, while settling behaviour can also vary greatly across different concentration ranges<sup>13</sup>. These vastly different settling regimes have great significance for industrial thickener performance, however a physical justification for these different hindered settling regimes remains uncertain.

Computational models have developed from the one dimensional batch sedimentation model for suspensions of incompressible, monodisperse spheres proposed in Kynch<sup>14</sup> to more complex suspensions of bidisperse<sup>15</sup> and polydisperse spheres<sup>4</sup>; however, suspensions of fine colloidal materials still represent a substantial modelling challenge for such computational approaches<sup>4</sup>. The scale of the challenge is further complicated by the fact that the size, shape and effective density of these aggregates in many industrial effluents are often poorly characterised<sup>16</sup> and can be highly dependent on the chemistry of the continuous phase<sup>10</sup> and on the shear environment of the suspension<sup>17-19</sup>. There is also evidence that larger aggregates are more fractal and less dense than smaller aggregates, due to the incorporation of large ratios of intra-aggregate fluid<sup>20,21</sup>, with the largest aggregates ( $>100\ \mu\text{m}$ ) often only marginally denser than the continuous phase<sup>21-23</sup>. Consequently, we rely on empirical settling models, such as those presented by Vesilind<sup>24</sup>, Richardson and Zaki<sup>25</sup>, Steinour<sup>26</sup>, Cho<sup>27</sup> and

Michaels and Bolger<sup>12</sup>, to imply the properties of the settling phase. However, these empirical models, discussed in more detail in the Theory section, require more extensive validation for aggregated suspensions using *in-situ* techniques for observing and measuring aggregates in suspension, such as Focused Beam Reflectance Measurements (FBRM)<sup>28,29</sup> and Particle Vision and Measurement (PVM)<sup>30,31</sup> techniques. Furthermore, if a structural model of the aggregates can be implied from settling behaviour, validated using these *in-situ* techniques, the opportunity arises to use this structural information to interpret the extreme transitions in settling behaviour across different concentration regimes, which are not currently well understood.

This complex sedimentation behaviour is examined here using aqueous suspensions of magnesium hydroxide,  $\text{Mg}(\text{OH})_2$ , which has previously attracted interest as it represents the limiting stage in its extraction from sea water<sup>32</sup> and brine by-products from coal mining<sup>33</sup>. However, magnesium hydroxide is also the primary corrosion product from Generation I spent nuclear fuel in the UK<sup>34</sup> which was clad with a *magnox* alloy of magnesium and small amounts of aluminium. Substantial volumes of  $\text{Mg}(\text{OH})_2$  rich intermediate level radioactive waste, called *corroded magnox sludge* (CMS), have accumulated in legacy ponds at the Sellafield nuclear decommissioning site in Cumbria, UK<sup>35,36</sup>. The time-line and expense of decommissioning ageing nuclear legacy buildings is highly dependent on the dewatering behaviour of  $\text{Mg}(\text{OH})_2$  rich suspensions, but any such spent nuclear fuel derivatives would require remote handling in a shielded *hot cell* for analysis. These handling limitations represent their own driver for deriving structural information for aggregated suspensions from remotely observed sedimentation behaviour. Hence it may be possible to optimise thickener design while minimising exposure to radiation workers.

This work uses a combination of *in-situ* and *ex-situ* particle characterisation technologies, such as PVM and flow particle image analysis (FPIA)<sup>37</sup> to develop a structural model for magnesium hydroxide. This structural model is used in conjunction with the Richardson and

Zaki<sup>25</sup>, Michaels and Bolger<sup>12</sup> and Valverde et al.<sup>6</sup> settling models to interpret the physical significance of the transition concentrations between different hindered settling regimes and the free settling velocities associated with each regime.

## Theory

Stokes' law<sup>38</sup> describes the terminal settling velocity,  $u_0$ , of a single hard sphere in an infinite fluid by equating the weight of the settling sphere with the viscous drag force:

$$u_0 = \frac{(\rho_p - \rho_f)}{18\eta} g d_p^2 \quad (1)$$

where  $\rho_p$  and  $\rho_f$  are the densities of particle and fluid phases,  $d_p$  is the particle size and  $g$  is acceleration due to gravity. For multi-particle suspensions, the Richardson and Zaki equation, Eq. (2),<sup>25</sup> represents the most popular empirical hindered settling model to accommodate the increased resistance to settling with increased solids concentration, or reduced porosity.

$$\frac{u}{u_0} = k (1 - \phi_p)^n \quad (2)$$

where  $u$  is the observed or *hindered* settling velocity,  $k$  is a dimensionless multiplier in the range  $0.8 < k \leq 1$  and  $n$  is the model exponent typically found in the range of 2-5<sup>25,39</sup>. An alternative empirical settling model is the Vesilind equation, Eq. (3)<sup>24</sup>, representing an exponential, rather than power law, relationship with solids concentration and is popular in the waste-water treatment industry<sup>40</sup>.

$$\frac{u}{u_0} = k e^{-n\phi_p} \quad (3)$$

Application of empirical hindered settling models to suspensions of fine aggregating minerals

reveals more complex settling behaviour. Table 1<sup>9,10,25,41</sup> reveals Richardson and Zaki exponents orders of magnitude greater for aggregated mineral suspensions than those typical for hard spheres. In addition, multiple settling regimes are observed with exponents roughly four times greater in the lower concentration regime.<sup>9</sup>

Table 1: Richardson and Zaki model parameters for hard spheres and aggregated mineral suspensions

Source	Material	Concentration range (% v/v)	Exponent	
Richardson and Zaki <sup>25</sup>	Uniform hard spheres	>4	2 - 5	
Alexander et al. <sup>10</sup>	Magnesium hydroxide	4.5-15.7	23.4	
Punnamaraju <sup>41</sup>		>1.1	259.4	
Bargiel and Tory <sup>9</sup>	Praseodymium oxalate	15.7-25.5	12.7	
		4.5-7.7	49.6	
		5.4-7.1	50.1	
Turian et al. <sup>11</sup>	Titanium dioxide	0.5-1.4	220.1	
		17.3-30.7	8.8	
		Laterite	3.6-12.7	24.6
		Gypsum	10.7-25.5	9.2

For aggregated mineral systems an unknown portion of the continuous phase is immobilised within the aggregates and so the effective occupancy of the suspension by aggregates,  $\phi_a$ , is greater than the concentration of the pure solid phase,  $\phi_p$ . Consequently, the Richardson and Zaki exponents for aggregated suspensions, reported in Table 1, could be artificially elevated due to the porosity not being adequately represented in the model. In order to quantitatively address this issue, the packing fraction of solids within the aggregate must be determined. The ratio between aggregate and primary particle volume fractions,  $C_{a/p}$ <sup>12</sup>, represents an inverse packing fraction of particles within the aggregate:

$$C_{a/p} = \frac{\phi_a}{\phi_p} = \frac{1}{\phi_{p/a}} \quad (4)$$

The effective porosity of the aggregate suspension,  $\varepsilon_a$ , is therefore:

$$\varepsilon_a = 1 - \phi_a = 1 - C_{a/p}\phi_p \quad (5)$$

A mass balance within the aggregate determines that the effective density driving force for settling aggregates is given by Eq. (6):

$$\rho_a - \rho_f = \frac{\rho_p - \rho_f}{C_{a/p}} \quad (6)$$

In a suspension of sufficiently low solids concentration, with a high inter-aggregate porosity, Michaels and Bolger<sup>12</sup> proposed that aggregates can be assumed to settle as non-interacting hard spheres<sup>12</sup>. There are limits to this assumption which will be addressed in more detail in the discussion. However, if the separation between aggregates is much greater than the range of van der Waals interactions, it is fair to conclude that comparable hydrodynamic hindering effects will control the sedimentation of aggregates and hard spheres.

By considering the analogy between settling aggregates and hard spheres, Eqs. (1) and (2) can be represented in terms of the aggregate diameter,  $d_a$ , the effective porosity,  $\phi_a$ , and the effective aggregate density,  $\rho_a$ . This provides the Michaels and Bolger<sup>12</sup> model, sometimes called a *modified Richardson and Zaki correlation*<sup>13</sup>, in Eq. (7):

$$\frac{u}{u_{a,0}} = k(1 - \phi_a)^n = k(1 - C_{a/p}\phi_p)^n \quad (7)$$

here the Stokes' settling velocity of an average aggregate,  $u_{a,0}$ , is given by Eq. (8):

$$u_{a,0} = (\rho_a - \rho_f) \frac{g\bar{d}_a^2}{18\eta} = \frac{(\rho_p - \rho_f)}{C_{a/p}} \frac{g\bar{d}_a^2}{18\eta} \quad (8)$$

In the low Reynolds number limit the Richardson and Zaki empirical constants,  $n$  and  $k$ , are typically taken to be 4.65 and 1 respectively<sup>25,39</sup>; Eq. (7) then linearises to Eq. (9):

$$u^{1/4.65} = u_{a,0}^{1/4.65} (1 - C_{a/p}\phi_p) \quad (9)$$

Hence a *Michaels and Bolger plot* can be used to estimate the free settling velocity of the aggregate from the y-intercept and the aggregate packing fraction from the x-intercept, from which Eq. (8) can provide a settling averaged aggregate diameter. Since a Richardson and Zaki exponent of 4.65 applies in the low Reynolds number limit ( $Re < 1$ )<sup>25,39</sup>, it is prudent to check that the exponent is appropriate based on the aggregate properties determined. Substituting the Stokes' settling velocity of the aggregate at infinite dilution into the definition of the Reynolds number yields Eq. (10):

$$Re_a = \frac{\rho_f u_{a,0} d_a}{\eta} = \frac{(\rho_p - \rho_f) \rho_f g \bar{d}_a^3}{18 C_{a/p} \eta^2} \quad (10)$$

A lower exponent should be applied for Reynolds numbers greater than unity as indicated in Eq. (11)<sup>25,39</sup>. The aggregate properties and particle Reynolds number should then be recalculated until the Reynolds number and exponent are in agreement.

$$\begin{aligned} n &\approx 4.65 \text{ at } Re \leq 1 \\ 2.5 \leq n &\leq 4.65 \text{ at } 1 < Re \leq 1000 \\ n &\approx 2.5 \text{ at } Re > 1000 \end{aligned} \quad (11)$$

This settling model is also adopted in Valverde et al.<sup>6</sup> using slightly different nomenclature. The inverse aggregate packing fraction is represented in terms of the ratio of mean aggregate diameter to primary particle diameter,  $\kappa = \frac{\bar{d}_a}{d_p}$ , and the mean number of primary particles

in an aggregate,  $N$ :

$$C_{a/p} = \frac{\frac{\pi}{6}\bar{d}_a^3}{N\frac{\pi}{6}d_p^3} = \frac{\kappa^3}{N} \quad (12)$$

The ratio of the free settling velocity of the aggregate to that of the primary particle,  $u_{p,0}$ , can also be represented in terms of  $\kappa$  and  $N$ :

$$\frac{u_{a,0}}{u_{p,0}} = \frac{\rho_a - \rho_f}{\rho_p - \rho_f} \frac{\bar{d}_a^2}{d_p^2} = \frac{N}{\kappa} \quad (13)$$

Using this nomenclature, Valverde et al.<sup>6</sup> express the Michaels and Bolger<sup>12</sup> equation as Eq. (14), using the slightly higher exponent of  $n = 5$ :

$$\frac{u}{u_{p,0}} = \frac{N}{\kappa} \left( 1 - \frac{\kappa^3}{N} \phi_p \right)^n \quad (14)$$

However, this amendment involves replacing the aggregate packing fraction with two unknown terms  $N$  and  $\kappa$ , and hence the model has a negative degree of freedom. This issue is addressed using the fact the unflocculated toner particles in Valverde et al.<sup>6</sup> have a very narrow size distribution and are considered monodisperse. Hence,  $N$  and  $\kappa$  can be calculated using either the Stokes' settling velocity of the monodisperse primary particles or the primary particle size using Eq. (15):

$$\begin{aligned} \kappa &= \frac{d_a}{d_p} = \sqrt{C_{a/p} \frac{u_{a0}}{u_{p0}}} \\ N &= \frac{d_a^3}{C_{a/p} d_p^3} = \kappa \frac{u_{a0}}{u_{p0}} \end{aligned} \quad (15)$$

# Experimental methods

## Materials

Versamag  $\text{Mg}(\text{OH})_2$  (Rohm and Haas, US) was used for settling and aggregation experiments. Versamag is a fine white precipitated powder with a density of  $2.36 \text{ g cm}^{-3}$  and solubility of  $6.9 \text{ mg l}^{-1}$  in water<sup>42</sup>. The Versamag test material contains trace amounts of magnesium and calcium oxides as impurities.

## Suspension preparation

2.1 l volume suspensions of  $\text{Mg}(\text{OH})_2$  in water were prepared in the concentration range of 0.7-6.5 % v/v for two parallel litre scale settling tests. The suspensions were agitated for 30 min with an axial flow impeller controlled by an overhead stirrer at 250 rpm. Suspension preparation was reduced to 0.7 l scale for settling tests using a Turbiscan LAb Expert (Formulation, Fr)<sup>43,44</sup> and increased to 7 l scale for particle characterisation using FBRM and PVM, using geometrically similar mixing vessels in each instance. Litre scale settling tests were conducted for 23 suspensions and a further 20 suspensions were investigated using the Turbiscan.

## Particle characterisation

Prior to investigating  $\text{Mg}(\text{OH})_2$  particles in suspension, zeta potential,  $\zeta$ , and pH were measured using a ZetaProbe (Colloidal Dynamics, USA)<sup>45</sup> to characterise the stability of magnesium hydroxide in aqueous environments. The sensitivity of aggregate sizes and shapes to their shear environment is well reported<sup>17,18</sup>, greatly complicating particle characterisation under realistic process conditions. Consequently, a combination of *ex-situ* and *in-situ*

techniques was employed to visualise and size particles across a range of shear conditions.

### ***Ex-situ* particle visualisation and sizing**

A Mastersizer 2000E (Malvern Instruments, UK)<sup>17</sup> was used to measure a particle size distribution (PSD) in a high shear environment. A dilute suspension was sonicated for 10 min prior to measurement in the Mastersizer, which itself used a high shear impeller at 2500 rpm to disperse particles and induce flow from the dispersion unit to the measurement window. It is assumed that the combined shear of the sonication and Mastersizer was sufficient to break down almost all large aggregates to their shear resistant constituent particles.

High resolution scanning electron microscope (SEM) images were captured of the dry Mg(OH)<sub>2</sub> powder, coated with 10 nm irridium, using an EVO MA15 (Carl Zeiss, Germany). Images were then captured of aggregates in suspension using a flow particle image analyzer (Sysmex FPIA-2100, Malvern Instruments, UK)<sup>37</sup>.

### ***In-situ* particle visualisation and sizing**

A Particle Vision and Measurement (PVM) instrument<sup>30,31</sup> (Mettler Toledo, US) was employed to capture images of aggregates under shear conditions more comparable to suspension preparation and settling conditions. A Focused Beam Reflectance Measurement (FBRM) probe (Mettler Toledo, US)<sup>18</sup> was used in parallel with the PVM in order to capture a chord length distribution (CLD) at 0.5 Hz measurement frequency. Both probes were mounted at a 45° angle to the impeller shaft in the mixing vessel to ensure representative flow of suspended particles past the measurement window<sup>31</sup>.

## Settling tests

### Litre scale settling tests

Suspensions were transferred to 1 l measuring cylinders, of 61 mm diameter, recalibrated to millimetre precision using adhesive measuring tape. The cylinders were inverted four times before commencing the settling tests. The height of the settling zonal suspension front (ZSF) was monitored as a function of time from visual measurements of the clarification point against the calibrated measuring tape.

### Turbiscan settling tests

Reduced scale settling tests were performed in tubes of 25 ml volume and 27.5 mm diameter using a Turbiscan LAb Expert (Formulation, Fr)<sup>43,44</sup>. The tubes were inverted four times prior to testing, while being careful to avoid introducing bubbles which would backscatter the Turbiscan light source.

The Turbiscan directs an 880 nm light source at a sample and measures a backscattering flux of light scattered by particles in the suspension. The backscattering flux,  $\Phi_{BS}$ , is inversely proportional to the root of the photon transport mean free path,  $\ell^*$ , which represents the average distance a photon travels through the dispersion before it diffuses away from its original trajectory. This mean free path is in turn inversely proportional to the volume fraction of particles and proportional to the mean particle diameter according to Mie theory:<sup>43</sup>

$$\Phi_{BS} \propto \sqrt{\frac{1}{\ell^*}} \quad (16)$$

and

$$\ell^*(d_p, \phi) = \frac{2d_p}{3\phi(1-\gamma)Q_s} \quad (17)$$

where  $\gamma$  is an asymmetry factor and  $Q_s$  represents a scattering efficiency factor. Assuming a fixed particle size distribution during settling, changes in backscattering flux correspond to changes in suspension concentration as a function of height and time. As the concentration of the suspension immediately below the clarification point remains constant<sup>46</sup>, analysis of the backscattering data can determine the height of the clarification point as a function of time. Equally, by monitoring the region of intense backscattering flux, growth of the sediment bed from the base of the tube can also be observed during testing. From the clarification interface height-time profiles for both litre scale and Turbiscan settling tests, the average settling velocities were estimated during the linear settling regime.

## Results and discussion

### Particle characterisation

Mg(OH)<sub>2</sub> suspensions displayed very low magnitude zeta potential measurements of 0.5-3.2 mV, indicative of weak electrostatic repulsion forces between particles in suspension. This implies that attractive van der Waals interactions are dominant and provide ample driving force for rapid aggregation<sup>13</sup>. Hence Mg(OH)<sub>2</sub> is a suitable test material to investigate the complex settling behaviour exhibited by aggregating suspensions summarised in Table 1. The suspensions self buffered to pH > 10 from very low solids concentrations, inhibiting calculation of the isoelectric point.

Images of Mg(OH)<sub>2</sub> were captured at three scales, shown in Figure 1, revealing three distinct particulate phases. The SEM image of the dry powder reveals hexagonal platelets of brucite,

referred to as *crystallites* in Li et al.<sup>47</sup>, with facial dimensions up to 400 nm and thicknesses less than 50 nm. In the SEM image, these platelets are clustered into a small *primary agglomerate* of around 3  $\mu\text{m}$  in diameter. These agglomerates of hexagonal platelet crystals are consistent with similar images in Gregson et al.<sup>34</sup> and Li et al.<sup>47</sup>.

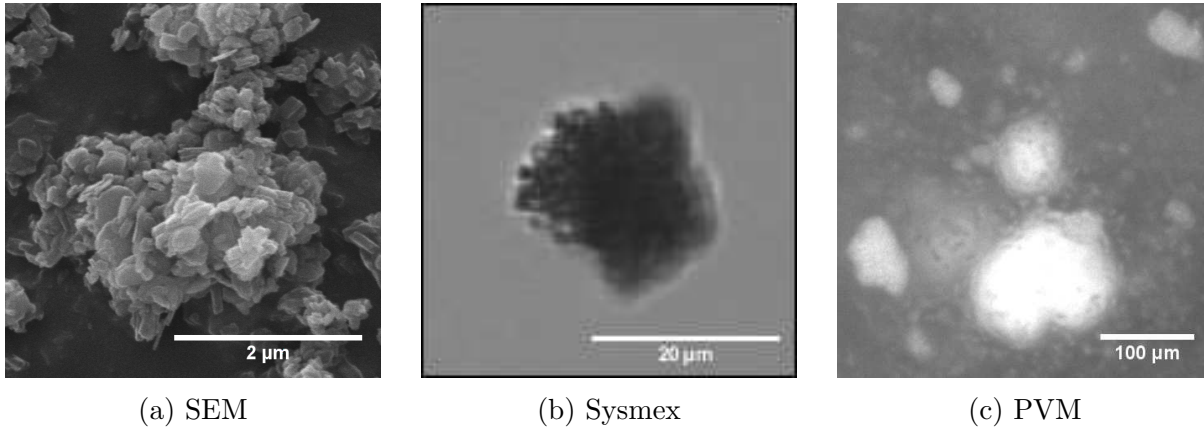


Figure 1: Images of  $\text{Mg}(\text{OH})_2$  at three scales

Figure 1b, captured using a Sysmex FPIA 2100, demonstrates the outline of these small primary agglomerates within a more irregular, fractal aggregate of 22  $\mu\text{m}$  diameter. The aggregate has a circularity of 0.59, which demonstrates the limitation of the assumption in Michaels and Bolger<sup>12</sup> that aggregates in dilute suspensions are analogous to hard spheres. Non-spherical particles tend to experience a greater drag force during settling and exhibit higher Richardson and Zaki exponents in the order of 5-6 in the low Reynolds number limit<sup>48</sup> than the typical exponent of 4.65 for spheres.

The primary agglomerates are not visible in the lower resolution PVM image in Figure 1c, but the size and polydispersity of the aggregates is clear. Figure 1c contains 85 aggregates greater than 1  $\mu\text{m}^2$  cross sectional area, the largest of which has an equivalent spherical diameter of 157  $\mu\text{m}$  and a hydrodynamic diameter, estimated from the smallest bounding circle around the two-dimensional aggregate image, closer to 180  $\mu\text{m}$ . Particles of this scale ( $> 100 \mu\text{m}$ ) are sometimes referred to as *macro-aggregates* and there is evidence in the literature<sup>20,21</sup> that these particles contain higher ratios of intra-aggregate fluid than smaller aggregates.

In some instances this greatly reduces the aggregate density until it is scarcely greater than that of the continuous phase<sup>21,22</sup>.

Michaels and Bolger<sup>12</sup> describe a similar structural model for kaolinite,  $\text{Al}_2\text{O}_3 \cdot 2\text{SiO}_2 \cdot 2\text{H}_2\text{O}$ , of hexagonal platelets with a length to thickness ratio of around 10, agglomerated into small, broadly spherical primary agglomerates which are able to resist shear breakdown. These agglomerates cluster to larger aggregates at low shear rates consistent with gravitational settling.

Using this interpretation of the various particle structures, a Malvern Mastersizer 2000E was used to capture the particle size distribution of primary agglomerates, shown in Figure 2, by imposing a very high shear on the suspension. The size distribution of 1-40  $\mu\text{m}$  is fairly broad, suggesting that some of the small and intermediate scale aggregates may have resisted shear breakdown, but the volume weighted  $d_{50}$  of 4.2  $\mu\text{m}$  is consistent with the scale of the primary agglomerate image in Figure 1a.

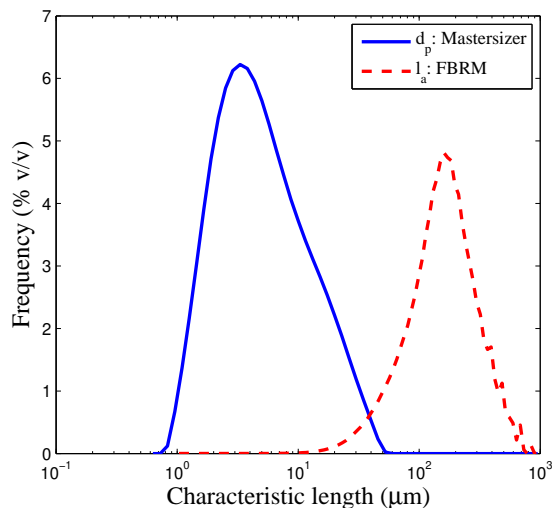


Figure 2:  $\text{Mg}(\text{OH})_2$  particle size distribution at high shear using a Mavern Mastersizer 2000 and a chord length distribution at low shear using a Mettler Toledo FBRM

The *ex-situ* Mastersizer PSD is contrasted with *in-situ* measurements captured using an FBRM probe in conditions more commensurate with the shear environment during suspen-

sion preparation for the settling tests. The FBRM CLD is not directly comparable with a PSD as chord lengths represent a complex function of particle size, shape, orientation and the co-ordinates of the FBRM laser path over the aggregate, but FBRM provides a good indication of the scale and polydispersity of the aggregates. The broad chord length distribution spans nearly two orders of magnitude, from a minimum size of around 20  $\mu\text{m}$ . Chord lengths greater than 200  $\mu\text{m}$  were ignored to remove potential data convolution with air bubbles, identified using the PVM, which persisted in suspensions agitated at the larger mixing scale. The resulting volume weighted median chord length,  $l_{50}$ , was found to be 152.4  $\mu\text{m}$ , similar to the largest aggregate pictured in Figure 1c and providing further evidence of the formation of macro-aggregates during suspension preparation. Table 2 summarises the structural model for  $\text{Mg}(\text{OH})_2$  based on this interpretation of the various *in-situ* and *ex-situ* measurements.

Table 2: Structural model for cohesive  $\text{Mg}(\text{OH})_2$

Particle phase	Scale	Evidence
Hexagonal platelet crystals	<400 nm face width <50 nm thickness	SEM images in Figure 1a and Gregson et al. <sup>34</sup> , Li et al. <sup>47</sup>
Primary agglomerates	$d_{50} \approx 4 \mu\text{m}$	Small cluster of platelets shown in the SEM image (Figure 1a), the smaller phase visible within the aggregate in the Sysmex image (Figure 1b) and the high shear Mastersizer PSD in Figure 2
Macro-aggregates	20-200 $\mu\text{m}$ $l_{50} \approx 152 \mu\text{m}$	PVM image in Figure 1c and FBRM CLD in Figure 2

## Suspension settling behaviour

Example hindered settling profiles from the 1 l measuring cylinder tests are shown for eight concentrations in Figure 3a and for two different concentrations from the Turbiscan tests in Figure 3b. Clear linear settling and compressional regimes are visible at both test scales, with the linear settling velocities decreasing with increased suspension concentration. From the litre scale settling profiles, the decrease in linear settling velocity with increasing concen-

tration is most significant in the 0.9-2.7 % v/v range, suggesting that there may be multiple hindered settling regimes.

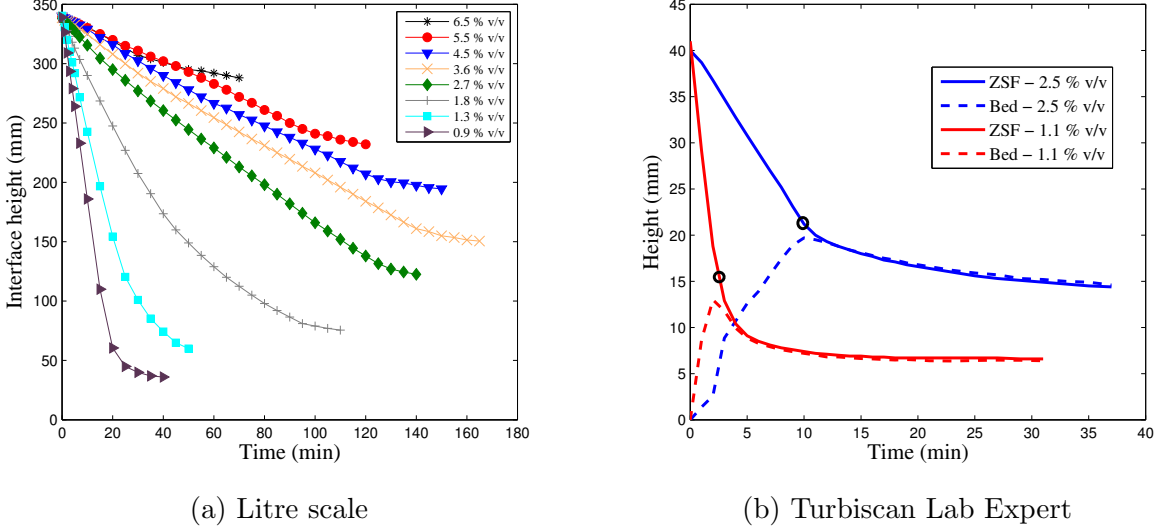


Figure 3: Example settling profiles for aqueous  $\text{Mg}(\text{OH})_2$  suspensions at two test scales; the transition point from linear settling to compressional dewatering is indicated by two circles in Figure 3b

The gel point,  $\phi_g$ , and final bed concentrations at the end of the batch settling tests,  $\phi_F$ , can be estimated on the basis that magnesium hydroxide is conserved below the settling interface, and hence no small solids remain suspended in the clarified zone. Using this assumption, the product of the instantaneous bulk concentration below the interface,  $\bar{\phi}(t)$ , and the volume of suspension below the interface,  $V(t)$ , provides the constant total volume of solids ( $\bar{\phi}(t)V(t) = \text{constant}$ ). The bulk concentration below the interface represents a spatial average and is hence distinct from the position dependent iso-concentration,  $\phi(H, t)$  immediately below the interface, which is estimated from tangents of the settling profile using Kynch theory<sup>14</sup>. Since the initial solids concentration,  $\phi$ , is known and the cross-sectional area of the settling cylinder is constant,  $\bar{\phi}(t)$  can be calculated from the instantaneous,  $H(t)$  and initial,  $H(0)$ , suspension heights according to Eq. (18):

$$\bar{\phi}(t) = \frac{H(0)}{H(t)}\phi \quad (18)$$

At the end of linear settling, indicated for two batch settling tests in Figure 3b, the suspensions below the interface are considered to be *gelled* and these networked suspensions then undergo a period of compressional dewatering. This is reflected in the dashed profiles of Figure 3b which show the rise of the bed from the base of the tube, similar to the experimental work in Holdich and Butt<sup>49</sup> and Hunter et al.<sup>50</sup>. The beds are observed to build during linear settling before undergoing a period of compression. The suspensions gel at concentrations of  $\phi_g = 5.4 \pm 1.6\% \text{ v/v}$  before compressing to final bed concentrations of  $\phi_F = 7.80 \pm 0.31\% \text{ v/v}$  at the end of the litre scale tests in Figure 3a. The settling profiles in Figure 3a are terminated within 3 h and so do not necessarily proceed to full equilibrium. Hence,  $\phi_F$  approaches an ultimate bed concentration but some further compression is anticipated. The two most concentrated suspensions investigated were initially above the gel point and therefore undergo compressional dewatering from the start of experimentation rather than hindered settling.

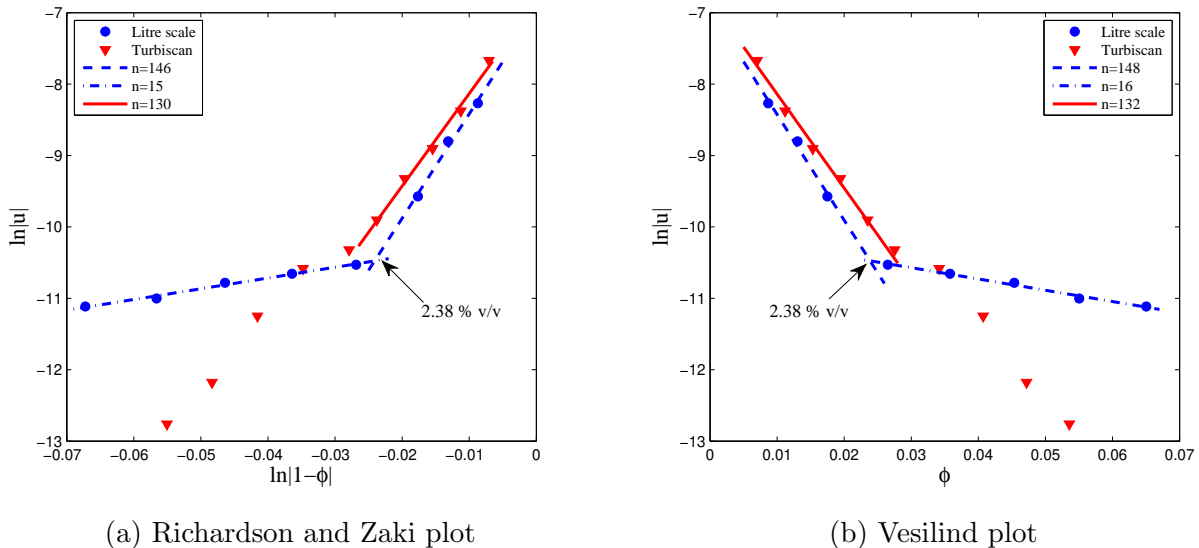


Figure 4: Conventional hindered settling models applied to  $\text{Mg}(\text{OH})_2$  suspensions at litre scale (blue) and 25 ml scale (red)

The linear settling velocities were extracted from the hindered settling data at both test

scales and were found in the range of 15-257  $\mu\text{m s}^{-1}$  for initial solids concentrations of 0.7-6.5 % v/v. By following the suspension preparation methodology outlined, the hindered settling profiles demonstrated good repeatability. The linear settling velocities of 9 hindered settling experiments at a concentration of 1.3 % v/v exhibited a standard deviation of 6.1 %. The average linear settling velocities at each concentration are presented in Richardson and Zaki<sup>25</sup> and Vesilind<sup>24</sup> plots in Figure 4 as the variation between experiments is too small to observe on logarithmic axes. The two plots appear almost as mirror images as  $\phi \approx -\ln|1-\phi|$  when  $\phi < 0.1$ . Both plots reveal two distinct regions of settling behaviour either side of a transition concentration of 2.38 % v/v for the litre scale settling data. The Richardson and Zaki<sup>25</sup> exponent of 146 in the lower concentration regime is amongst the largest reported in the literature, as shown in Table 1, and is over thirty times greater than a typical exponent associated with settling hard spheres<sup>25,39</sup>. The disparity between the two concentration regimes is also greater than reported elsewhere in the literature<sup>9,12</sup>. Exponents are roughly four times larger in the more concentrated regimes for calcium carbonate and praseodymium oxalate in Bargiel and Tory<sup>9</sup>, whereas the low concentration regime exponent for  $\text{Mg}(\text{OH})_2$  is an order of magnitude greater than that of 15 observed in the more concentrated regime.

The reason for these multiple settling regimes for aggregated suspensions and the physical significance of the transition concentration remains uncertain. Michaels and Bolger<sup>12</sup> observed a change in hindered settling behaviour for kaolinite at 0.7 % v/v which was explained by the formation of chains and networks of aggregates above this threshold concentration. This appears a very low concentration to mark the formation of these macro-structures within the suspension, and the theory would require very high ratios of intra-aggregate fluid to explain the onset of inter-aggregate bonding at such a low concentration.

Allain et al.<sup>13</sup> proposed two critical concentrations, labelled  $\phi^*$  and  $\phi^{**}$ , found at 0.3 % v/v and 5 % v/v for the calcium carbonate test material used in the study. The former is said to represent the transition from the deposition of discrete aggregates to *collective settling* while

the latter marks the cessation of hindered settling and onset of compressional dewatering. The later description defines the gel point of the suspension and is henceforth labelled  $\phi_g$ . The lower of the two critical concentrations,  $\phi^*$ , appears to mark the transition between the two hindered settling regimes observed here and discussed in Michaels and Bolger<sup>12</sup>. Terms such as collective settling, colloidal gels and gelled suspensions may be somewhat misleading for suspensions at concentrations significantly below the gel point. Suspensions in the high concentration regime still exhibit linear settling rather than the compressional dewatering associated with fully gelled suspensions.

The departure between the two settling regimes, observed in Figure 4, is further demonstrated by the variation in hindered settling velocities at the two experimental scales. There is reasonably good agreement demonstrated between the two test scales within the low concentration settling regime, however significantly slower settling velocities are observed in the reduced scale Turbiscan tests at concentrations above 3.6 % v/v (Figure 4). This could be explained by bridging effects across the smaller diameter Turbiscan vial, similar to those discussed in Buratto et al.<sup>51</sup>, by the additional height of the litre scale tests promoting greater compression and also by the larger cross-sectional area of the litre scale cylinders facilitating more extensive channelling. Given this discrepancy between the experimental scales, care should be taken to use the Turbiscan at suspension concentrations below  $\phi^*$  where the settling dynamics are not so influenced by severe wall effects.

Kynch<sup>14</sup> theory enables the calculation of isoconcentration ( $\phi(H, t)$ ) lines and corresponding settling velocities,  $u(\phi)$ , from tangents to the interface height-time profile, as discussed in Usher et al.<sup>52</sup>. The product of the tangent velocity and corresponding isoconcentration, expressed as a density,  $\rho(H, t)$ , provides a mass flux,  $\Psi(\phi)$ , of settling solids through the cylinder.

$$\Psi(\phi) = u(\phi)\rho(H, t) \tag{19}$$

This analysis was applied to the two Turbiscan profiles in Figure 3b and the litre scale tests of lowest initial concentration in Figure 3b, as shown in Figure 5. The mass flux calculations during linear settling are also shown for all settling tests at both experimental scales. The disparity between the two experimental scales is much less apparent when analysed in terms of mass flux than using Richardson and Zaki<sup>25</sup> analysis of the hindered settling velocities. However, the concentration of 2.38 % v/v ascribed to  $\phi^*$  in Figure 4a appears equally significant in Figure 5. The low concentration regime is characterised by a rapid fall in mass flux with increased concentration, while the mass flux above  $\phi^*$  remains relatively constant and below a value of  $0.04 \text{ kg m}^2 \text{ s}^{-1}$ . The maximum of the mass flux-concentration profile appears to correspond to a more dilute suspension than those investigated. Suspensions below 0.7 % v/v concentration exhibited extremely rapid settling velocities and optically vague clarification points which inhibited data collection at the very dilute limit.

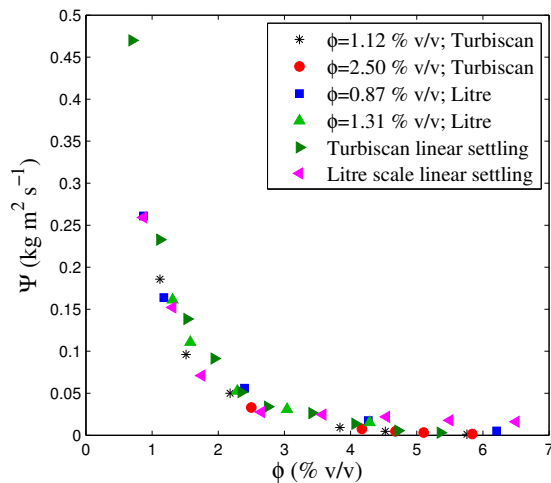


Figure 5: The mass flux of settling solids at two experimental settling scales using Kynch theory

One of the advantages of using empirical hindered settling models is that they enable extrapolation to the point of infinite dilution (at the y-intercept) providing a characteristic free settling velocity from which the particle size can be estimated. The existence of multiple settling regimes necessitates the existence of more than one y-intercept and hence more than one free settling velocity. The free settling velocities extrapolated from each concentration

regime, at each experimental scale and using each empirical model are shown in Figure 6.

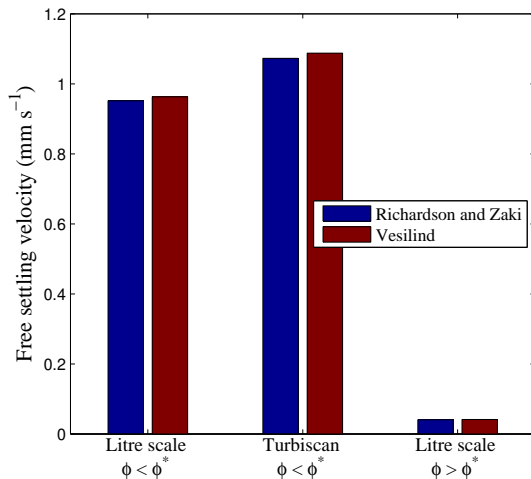


Figure 6: Free settling velocities predicted from the Richardson and Zaki and Vesilind models for the low ( $\phi < \phi^*$ ) and high ( $\phi > \phi^*$ ) concentration settling regimes

For each experimental scale and settling regime the difference between the free settling velocities predicted from the Richardson and Zaki and Vesilind plots is negligible, but the Vesilind free settling velocities are marginally greater in each instance. The free settling velocities within the low concentration regime are 13% higher for the Turbiscan tests than the litre scale tests, but the two experimental scales are in reasonable agreement given the difficulties associated with scaling down suspension preparation for the Turbiscan tests<sup>44</sup>. The free settling velocities extrapolated from the high concentration regime are over 23 times lower than for the low concentration regime, however it remains difficult to derive meaning from the free settling velocity extrapolated from the high concentration regime without understanding the transition that takes place at  $\phi^*$ .

If the low concentration regime represents suspensions of discrete, disperse aggregates then the free settling velocity represents the Stokes' settling velocity of an aggregate,  $u_{a0}$ . A free settling velocity would typically be used to interpret the size of the settling phase, however Stokes' law cannot be solved in the absence of a known particle density. The aggregate density must exist between the bounding densities of water and  $\text{Mg}(\text{OH})_2$  as defined by

Eq. (20).

$$\rho_a = \frac{\rho_p + (C_{a/p} - 1)\rho_f}{C_{a/p}} \quad (20)$$

At very low packing fractions, the aggregate density would approach that of the continuous phase where there is little or no density driving force for settling, hence the estimated aggregate size will appear to be infinitely large. If the aggregate density approaches that of pure  $\text{Mg}(\text{OH})_2$ , this provides a minimum bound for the predicted aggregate size. The free settling velocities extrapolated from the low concentration regime using the Richardson and Zaki<sup>25</sup> and Vesilind<sup>24</sup> models correspond to minimum particle diameters of 27.2 and 27.4  $\mu\text{m}$  respectively based on the litre scale batch settling data. However, in reality the aggregate density will be lower than that of pure  $\text{Mg}(\text{OH})_2$  and for a more precise estimation of aggregate size the Michaels and Bolger<sup>12</sup> model is employed to estimate the packing fraction within the aggregate. First Figures 4a and 4b are used to discard the settling data above  $\phi^*$  as Michaels and Bolger<sup>12</sup> analysis is limited to the low concentration regime of disperse aggregates. The remaining linear settling velocities are presented in Figure 7.

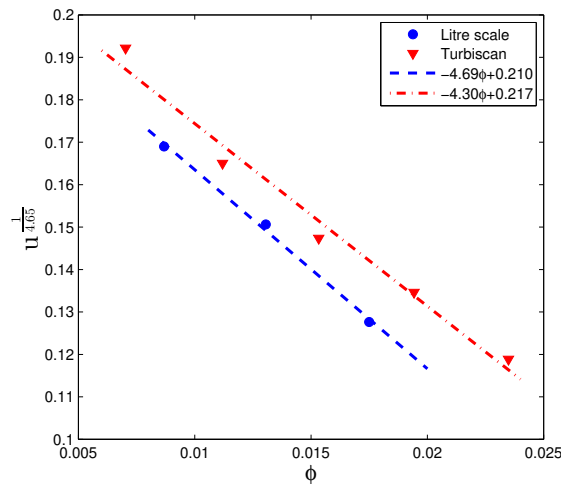


Figure 7: Michaels and Bolger plot for  $\text{Mg}(\text{OH})_2$  suspensions at litre scale (blue) and 25 ml scale (red)

The two scales of settling data fit very well using an exponent value of 4.65, with residuals of  $R^2 > 0.979$ . The linear fits presented in the legend rearrange to the form of Eq. (7), as shown in Eq. (21):

$$\begin{aligned} \frac{u}{7.11e-04} &= (1 - 22.3\phi)^{4.65} \text{ at litre scale} \\ \frac{u}{8.29e-04} &= (1 - 19.8\phi)^{4.65} \text{ at Turbiscan scale} \end{aligned} \quad (21)$$

where the denominator on the left hand side represents a modified aggregate free settling velocity and the multiplier of the solids volume fraction represents the inverse packing fraction within the aggregate. From these linear fits, the intra-aggregate packing fractions are estimated at 0.045-0.051, corresponding to aggregate densities of just 1059-1067 kg m<sup>-3</sup>, and thus relatively close to the density of water. At first glance the packing fractions appear surprisingly low, however low density *macro-aggregates* (>150 μm) with densities only around 50-100 kg m<sup>-3</sup> greater than water have been discussed in the literature<sup>17-21,53</sup>.

The aggregate free settling velocity and packing fraction were used to estimate the average aggregate diameters using Eq. (8). A summary of the estimated aggregate properties is provided in Table 3. Sensitivity analysis of the Michaels and Bolger<sup>12</sup> approach has been included using a slightly larger exponent of 6, which is more typical for non-spherical particles which experience greater drag<sup>48</sup>. The Valverde et al.<sup>6</sup> aggregate parameters,  $N$  and  $\kappa$ , were estimated using an assumed primary agglomerate size of 4.2 μm based on the median particle size obtained using the Malvern Mastersizer.

The average aggregate properties determined from the Michaels and Bolger<sup>12</sup> model (Table 3) correspond to aggregate Reynolds numbers at infinite dilution of 0.1 and 0.12 at litre and Turbiscan scales respectively, justifying the use of exponents (4.65-6) associated with the low Reynolds number limit (Eq. (11)). The calculated aggregate diameters of 146.2-148.7 μm appear realistic based on the FBRM CLD presented in Figure 2, which had a volume weighted

Table 3: Settling and structural parameters determined from the low concentration regime using various hindered settling models

Model	Data	n	$u_{a,0}$ (m/s)	$C_{a/p}$	$d_a$ ( $\mu\text{m}$ )	$\kappa$	$N$	$\rho_a$ ( $\text{kg}/\text{m}^3$ )
Richardson and Zaki	litre scale	146	$9.52 \times 10^{-4}$	-	>27.2	-	-	-
	Turbiscan	130	$1.07 \times 10^{-3}$	-	>28.9	-	-	-
Vesilind	litre scale	148	$9.63 \times 10^{-4}$	-	>27.4	-	-	-
	Turbiscan	132	$1.09 \times 10^{-3}$	-	>29.1	-	-	-
Michaels and Bolger	litre scale	4.65	$7.11 \times 10^{-4}$	22.3	146.2	35	1892	1059
	Turbiscan	4.65	$8.29 \times 10^{-4}$	19.8	148.7	35	2242	1067
Michaels and Bolger (sensitivity analysis)	litre scale	6	$7.52 \times 10^{-4}$	18.5	137.1	32	1877	1072
	Turbiscan	6	$8.71 \times 10^{-4}$	16.5	139.0	33	2203	1081

median chord length of  $152.4 \mu\text{m}$ . Aggregate dimensions in the order of  $150 \mu\text{m}$  are also consistent with the largest aggregate shown in the PVM image in Figure 1c. Settling averaged particle sizes for polydisperse suspensions can be weighted in favour of larger particles as smaller particles experience reduced drag in the wake of larger particles.

Investigating the Michaels and Bolger<sup>12</sup> approach using a higher exponent of 6 resulted in the prediction of a marginally smaller and denser aggregate of  $137.1\text{-}139.0 \mu\text{m}$  diameter and  $1072\text{-}1081 \text{ kg m}^{-3}$  density, however the aggregate properties were shown to be not especially sensitive to changes in the exponent within the  $4.65\text{-}6$  range. The predicted free settling velocities increased by about 5% when using the higher exponent of 6, but are still around 25% lower than those predicted using the conventional Richardson and Zaki<sup>25</sup> and Vesilind<sup>24</sup> approaches, shown in Figure 6.

A series of critical concentrations, obtained from the batch settling data, are summarised in Table 4. The transitions from linear settling to compressional dewatering are marked in Figure 3b, demonstrating the calculation of the gel point using Eq. (18). The same approach is applied for the litre scale settling data and presented in Table 4:

The low aggregate packing fractions mean the solids concentration at the transition point

Table 4: Critical concentrations observed from the hindered settling of magnesium hydroxide

	$\phi$	$\phi^*$	$\phi_g$	$\phi_F$	$\phi_{p/a}$
1 litre	0.009-0.065	0.024	$0.054 \pm 0.016$	$0.078 \pm 0.003$	0.045
Turbiscan	0.007-0.054	-	$0.049 \pm 0.010$	$0.075 \pm 0.011$	0.051

( $\phi^* = 2.38\% \text{ v/v}$ ) corresponds to an aggregate concentration,  $\phi_a^* = C_{a/p}\phi^*$ , of 47-53% v/v. If aggregates occupy at least half the suspension within the high concentration regime, inter-aggregate separation may approach the range of van de Waals forces and some of the macro-features discussed in Michaels and Bolger<sup>12</sup>, such as aggregate chains, could be feasible. However, there is currently no experimental evidence to corroborate the presence of these large structures within the high concentration regime.

Table 4 demonstrates that the intra-aggregate packing fraction,  $\phi_{p/a}$ , approximates the experimental gel point,  $\phi_g$ , characterised by the onset of compressional dewatering in Figure 3. This implies that the aggregates would have to undergo some densification within the high concentration settling regime as even optimum close packing of the low density aggregates would necessitate a gel point lower than the intra-aggregate packing fraction and no greater than 0.04. This is reinforced by Buratto et al.<sup>51</sup>, which suggests that shear densification of aggregates is a realistic mechanism for dewatering even within the mild shear environment of a gravitational settling column. If aggregates undergo simultaneous dewatering along with the bulk suspension then the properties of the primary agglomerates, rather than the properties of the larger aggregates, will increasingly control the descension of the clarification interface. Assuming that the rate of dewatering is controlled by the much smaller dimensions of the primary agglomerates would explain why the free settling velocity extrapolated from the high concentration regime is 23 times lower than that obtained from the low concentration settling data, as demonstrated in Figure 6.

If aggregates are subject to dewatering when the aggregates occupy a majority of the initial suspension, this is not observed in the late stages of linear settling in suspensions of low initial

solids concentrations, when aggregates also occupy a majority of the suspension below the clarification point. There are a number of reasons this could be the case. First, Gaudin and Fuerstenau<sup>46</sup> argue that the concentration immediately below the settling interface remains constant and approximate to the initial suspension concentration; this would explain why a constant, linear settling velocity is observed until gellation. Second, the large terminal settling velocity of these macro-aggregates means that the period between 50% aggregate occupation of the suspension and the onset of compression is much more brief (< 10 min) than the severely hindered high initial concentration suspensions where linear dewatering persists for up to 2 h (Figure 3a). This may not enable sufficient time for aggregate restructuring. Third, the rapid settling rates of macro-aggregates in low initial concentration suspensions may promote fluid flow past aggregates rather than through aggregates; as such, high velocity macro-aggregates may exhibit less porous behaviour.

Hence, it is clear that complex settling dynamics control the rate of dewatering between the first threshold concentration and the gel point. Further work is required to couple aggregate densification with aggregate settling to adequately model this high concentration regime but it appears the dimensions of small dense primary agglomerates rather than those of large, loosely bound macro-aggregates are significant in governing this complex settling behaviour when aggregates occupy at least 50% of the initial suspension volume.

## Conclusions

Aqueous suspensions of magnesium hydroxide have been shown to exhibit significantly different settling dynamics within two distinct concentration regimes. The Richardson and Zaki<sup>25</sup> exponent is a factor of 10 larger below a threshold concentration of  $\phi^* = 2.38\% \text{ v/v}$ , while the free settling velocity extrapolated from the higher concentration regime is 23 times lower than that associated with the low concentration regime. This disparity is much greater than

that previously reported for other low zeta potential mineral suspensions, such as kaolinite<sup>12</sup> and calcium carbonate<sup>9</sup>.

Below the transition concentration it is believed that settling is governed by fluid flow past discrete, disperse aggregates. A Michaels and Bolger<sup>12</sup> analysis predicted large aggregate dimensions of 137-149  $\mu\text{m}$  diameter, which is consistent with *in-situ* images and chord lengths obtained using PVM and FBRM respectively. These *macro-aggregates* would have very low packing fractions, 4.5-5.1 % v/v, similar to the gel point of around 5.2-5.6 % v/v, and so their densities, 1050-1080  $\text{kg m}^{-3}$ , are only marginally greater than the continuous phase. The loose packing within the aggregates also implies that aggregates would occupy at least half the volume of suspensions above the transition concentration.

The close similarity between the intra-aggregate packing fraction and the gel point implies that the aggregates undergo some densification prior to gellation as perfect aggregate packing at the end of linear settling would be unrealistic. Images obtained using SEM and a Flow Particle Image Analyser confirm that the larger aggregates contain a smaller phase of primary agglomerates, while a Malvern Mastersizer particle size distribution obtained under very high shear conditions implied a median primary agglomerate size of 4.2  $\mu\text{m}$ . Shear densification of aggregates means that fluid flow past these small primary agglomerates may control the rate of dewatering in the higher concentration regime rather than flow past large macro-aggregates.

## Acknowledgements

Thank you to Sellafield Ltd. and the Nuclear Decommissioning Authority (NDA) for funding this work through an Engineering and Physical Sciences Research Council (EPSRC) industrial case award (grant reference: EP/K504440). We also thank Geoff Randall and Martyn

Barnes of Sellafield Ltd. for their support of this research.

## Nomenclature

$\ell^*$	Photon transport mean free path
$\eta$	Viscosity (Pa s)
$\gamma$	Asymmetry factor
$\kappa$	Aggregate diameter ratio
$\phi$	Volume fraction
$\Phi_{BS}$	Backscattering flux
$\Psi$	Mass flux of solids
$\rho$	Density ( $\text{kg m}^{-3}$ )
$C$	Packing fraction
$d$	Diameter (m)
$g$	Acceleration due to gravity ( $\text{m s}^{-1}$ )
$H$	Settling suspension height (m)
$k$	Empirical model multiplier
$N$	Number of primary agglomerates in an aggregate
$n$	Empirical model exponent
$Q_s$	Scattering efficiency factor

$Re$	Reynolds number ( $\frac{\rho u d}{\eta}$ )
$u$	Settling velocity ( $\text{m s}^{-1}$ )
$V$	Settling suspension volume ( $\text{m}^3$ )

### Subscripts and superscripts

0	at infinite dilution
$a$	aggregate
*	settling transition point
$F$	final
$f$	fluid
$g$	gel point
$p$	particle or primary agglomerate

### References

1. Usher, S.; Spehar, R.; Scales, P. Theoretical analysis of aggregate densification: impact on thickener performance. *Chem. Eng. J.* **2009**, *151*, 202–208.
2. D. Stickland, A.; Burgess, C.; Dixon, D.; Harbour, P.; Scales, P.; Studer, L.; Usher, S. Fundamental dewatering properties of wastewater treatment sludges from filtration and sedimentation testing. *Chem. Eng. Sci.* **2008**, *63*, 5283–5290.
3. Manning, A. Observations of the properties of flocculated cohesive sediment in three western European estuaries. *J. Coastal Res.* **2004**, 70–81.

4. Concha, F.; Bustos, M. Modification of the Kynch theory of sedimentation. *AIChE J.* **1987**, *33*, 312–315.
5. Castellanos, A.; Valverde, J.; Quintanilla, M. Aggregation and sedimentation in gas-fluidized beds of cohesive powders. *Phys. Rev. E* **2001**, *64*, 041304.
6. Valverde, J. M.; Quintanilla, M. A. S.; Castellanos, A.; Mills, P. The settling of fine cohesive powders. *Europhys. Lett.* **2001**, *54*, 329–334.
7. Vesaratchanon, J.; Nikolov, A.; Wasan, D. T. Collective particle interactions in the sedimentation of charged colloidal suspensions. *Ind. Eng. Chem. Res.* **2009**, *48*, 80–84.
8. Hunter, R. J. The flow behavior of coagulated colloidal dispersions. *Adv. Colloid Interface Sci.* **1982**, *17*, 197–211.
9. Bargiel, M.; Tory, E. M. Extension of the Richardson-Zaki equation to suspensions of multisized irregular particles. *Int. J. Miner. Process.* **2013**, *120*, 22–25.
10. Alexander, K. S.; Dollimore, D.; Tata, S. S.; Uppala, V. Comparison of the coefficients in the Richardson and Zaki's and Steinour's equations relating to the behavior of concentrated suspensions. *Sep. Sci. Technol.* **1991**, *26*, 819–829.
11. Turian, R.; Ma, T.; Hsu, F.; Sung, D. Characterization, settling, and rheology of concentrated fine particulate mineral slurries. *Powder Technol.* **1997**, *93*, 219–233.
12. Michaels, A. S.; Bolger, J. C. Settling rates and sediment volumes of flocculated kaolin suspensions. *Ind. Eng. Chem. Fundam.* **1962**, *1*, 24–33.
13. Allain, C.; Cloitre, M.; Wafra, M. Aggregation and sedimentation in colloidal suspensions. *Phys. Rev. Lett.* **1995**, *74*, 1478–1481.
14. Kynch, G. A theory of sedimentation. *Trans. Faraday Soc.* **1952**, *48*, 166–176.

15. Dorrell, R.; Hogg, A. Sedimentation of bidisperse suspensions. *Int. J. Multiphase Flow* **2010**, *36*, 481–490.
16. Hildred, K.; Townson, P.; Hutson, G.; Williams, R. Characterisation of particulates in the BNFL enhanced actinide removal plant. *Powder Technol.* **2000**, *108*, 164–172.
17. Biggs, C.; Lant, P. Activated sludge flocculation: on-line determination of floc size and the effect of shear. *Water Res.* **2000**, *34*, 2542–2550.
18. Owen, A.; Fawell, P.; Swift, J.; Labbett, D.; Benn, F.; Farrow, J. Using turbulent pipe flow to study the factors affecting polymer-bridging flocculation of mineral systems. *Int. J. Miner. Process.* **2008**, *87*, 90–99.
19. Gladman, B.; de Kretser, R.; Rudman, M.; Scales, P. Effect of shear on particulate suspension dewatering. *Chem. Eng. Res. Des.* **2005**, *83*, 933–936.
20. Gibbs, R. Estuarine flocs: their size, settling velocity and density. *J. Geophys. Res.* **1985**, *90*, 3249–3251.
21. Glover, S. M.; Jameson, G. J.; Biggs, S. Bridging flocculation studied by light scattering and settling. *Chem. Eng. J.* **2000**, *80*, 3–12.
22. Dyer, K.; Manning, A. Observation of the size, settling velocity and effective density of flocs, and their fractal dimensions. *J. Sea Res.* **1999**, *41*, 87–95.
23. Manning, A.; Dyer, K. A laboratory examination of floc characteristics with regard to turbulent shearing. *Mar. Geol.* **1999**, *160*, 147–170.
24. Vesilind, A. Design of prototype thickeners from batch settling tests. *Water Sewage Works* **1968**, *115*, 302–307.
25. Richardson, J. F.; Zaki, W. N. The sedimentation of a suspension of uniform spheres under conditions of viscous flow. *Chem. Eng. Sci.* **1954**, *3*, 65–73.

26. Steinour, H. H. Rate of sedimentation: nonfocculated suspensions of uniform spheres. *Ind. Eng. Chem.* **1944**, *36*, 618–624.
27. Cho, S.; Colin, F.; Sardin, M.; Prost, C. Settling velocity model of activated sludge. *Water Res.* **1993**, *27*, 1237–1242.
28. Peng, S.; Williams, R. Control and optimisation of mineral flocculation and transport processes using on-line particle size analysis. *Miner. Eng.* **1993**, *6*, 133–153.
29. Barrett, P.; Glennon, B. In-line FBRM monitoring of particle size in dilute agitated suspensions. *Part. Part. Syst. Charact.* **1999**, *16*, 207–211.
30. Greaves, D.; Boxall, J.; Mulligan, J.; Montesi, A.; Creek, J.; Dendy Sloan, E.; Koh, C. Measuring the particle size of a known distribution using the focused beam reflectance measurement technique. *Chem. Eng. Sci.* **2008**, *63*, 5410–5419.
31. Barrett, P.; Glennon, B. Characterizing the metastable zone width and solubility curve using lasentec FBRM and PVM. *Chem. Eng. Res. Des.* **2002**, *80*, 799–805.
32. Petric, B.; Petric, N. Investigations of the rate of sedimentation of magnesium hydroxide obtained from sea water. *Ind. Eng. Chem. Process Des. Dev.* **1980**, *19*, 329–335.
33. Turek, M.; Gnot, W. Precipitation of magnesium hydroxide from brine. *Ind. Eng. Chem. Res.* **1995**, *34*, 244–250.
34. Gregson, C. R.; Goddard, D. T.; Sarsfield, M. J.; Taylor, R. J. Combined electron microscopy and vibrational spectroscopy study of corroded Magnox sludge from a legacy spent nuclear fuel storage pond. *J. Nucl. Mater.* **2011**, *412*, 145–156.
35. Jackson, S.; Monk, S.; Riaz, Z. An investigation towards real time dose rate monitoring, and fuel rod detection in a First Generation Magnox Storage Pond (FGMSP). *Appl. Radiat. Isot.* **2014**, *94*, 254–259.

36. Gregson, C.; Hastings, J.; Sims, H.; Steele, H.; Taylor, R. Characterisation of plutonium species in alkaline liquors sampled from a UK legacy nuclear fuel storage pond. *Analytical Methods* **2011**, *3*, 1957–1968.
37. Komabayashi, T.; Spångberg, L. S. Comparative analysis of the particle size and shape of commercially available mineral trioxide aggregates and Portland cement: A Study with a Flow Particle Image Analyzer. *Journal of Endodontics* **2008**, *34*, 94–98.
38. Stokes, G. On the effect of the internal friction of fluids on the motion of pendulums. *Cambridge Philos. Soc.*, [reprinted in *Mathematical and Physical Papers 3, 1-86*] **1850**, *IX*, 8.
39. Winterwerp, J.; Van Kesteren, W. G. M. *Introduction to the physics of cohesive sediment dynamics in the marine environment*; Dev. Sedimentol.; 2004; Vol. 56; pp 397–466.
40. Zhang, D.; Li, Z.; Lu, P.; Zhang, T.; Xu, D. A method for characterizing the complete settling process of activated sludge. *Water Res.* **2006**, *40*, 2637–2644.
41. Punnamaraju, S. R. The evaluation of the sedimentation behavior of magnesium hydroxide in the never dried state. M.Sc. thesis, The University of Toledo, 2012.
42. Magnesium hydroxide MSDS, CAS # 1309-42-8. Martin Marietta Magnesia Specialties, 2014.
43. Celia, C.; Trapasso, E.; Cosco, D.; Paolino, D.; Fresta, M. Turbiscan Lab Expert analysis of the stability of ethosomes and ultradeformable liposomes containing a bilayer fluidizing agent. *Colloids Surf., B* **2009**, *72*, 155–160.
44. Bux, J.; Peakall, J.; Biggs, S.; Hunter, T. N. In situ characterisation of a concentrated colloidal titanium dioxide settling suspension and associated bed development: Application of an acoustic backscatter system. *Powder Technol.* **2015**, *284*, 530–540.

45. Hidalgo-Ivarez, R.; Martn, A.; Fernndez, A.; Bastos, D.; Martnez, F.; de las Nieves, F. Electrokinetic properties, colloidal stability and aggregation kinetics of polymer colloids. *Adv. Colloid Interface Sci.* **1996**, *67*, 1–118.
46. Gaudin, A.; Fuerstenau, M. The transviewer-x rays to measure suspended solids concentration. *Eng. Min. J.* **1958**, *159*, 110–112.
47. Li, X.; Ma, G. B.; Liu, Y. Y. Synthesis and characterization of magnesium hydroxide using a bubbling setup. *Ind. Eng. Chem. Res.* **2009**, *48*, 763–768.
48. Chong, Y. S.; Ratkowsky, D. A.; Epstein, N. Effect of particle shape on hindered settling in creeping flow. *Powder Technol.* **1979**, *23*, 55–66.
49. Holdich, R.; Butt, G. Compression and channelling in gravity sedimenting systems. *Miner. Eng.* **1996**, *9*, 115 – 131.
50. Hunter, T. N.; Usher, S. P.; Biggs, S.; Scales, P. J.; Stickland, A. D.; Franks, G. V. Characterization of bed densification in a laboratory scale thickener, by novel application of an acoustic backscatter system. *Procedia Engineering* **2015**, *102*, 858 – 866.
51. Buratto, B.; Usher, S. P.; Parris, D.; Scales, P. J. Wall effects during settling in cylinders. *Colloids Surf., A* **2014**, *449*, 157 – 169.
52. Usher, S. P.; Studer, L. J.; Wall, R. C.; Scales, P. J. Characterisation of dewaterability from equilibrium and transient centrifugation test data. *Chem. Eng. Sci.* **2013**, *93*, 277–291.
53. MacDonald, I. T.; Vincent, C. E.; Thorne, P. D.; Moate, B. D. Acoustic scattering from a suspension of flocculated sediments. *J. Geophys. Res.: Oceans* **2013**, *118*, 2581–2594.

# Table of contents graphic

